

Experimental observations on the effect of interface slip on rotation and stabilisation of rigid particles in simple shear and a comparison with natural mylonites.

Neil S. Mancktelow, Laurent Arbaret, Giorgio Pennacchioni

▶ **To cite this version:**

Neil S. Mancktelow, Laurent Arbaret, Giorgio Pennacchioni. Experimental observations on the effect of interface slip on rotation and stabilisation of rigid particles in simple shear and a comparison with natural mylonites.. Journal of Structural Geology, 2002, 24, pp.567-585. 10.1016/S0191-8141(01)00084-0 . hal-00072749

HAL Id: hal-00072749
https://insu.hal.science/hal-00072749

Submitted on 26 Aug 2011

HAL is a multi-disciplinary open access archive for the deposit and dissemination of scientific research documents, whether they are published or not. The documents may come from teaching and research institutions in France or abroad, or from public or private research centers.

L'archive ouverte pluridisciplinaire **HAL**, est destinée au dépôt et à la diffusion de documents scientifiques de niveau recherche, publiés ou non, émanant des établissements d'enseignement et de recherche français ou étrangers, des laboratoires publics ou privés.

Rotational behaviour of rigid particles in simple shear: experimental and natural observations on stabilization due to interface slip

Neil S. Mancktelow[a], Laurent Arbaret[b], Giorgio Pennachioni[c]

a. Geologisches Institut, ETH-Zentrum, CH-8092 Zürich, Switzerland

b. UFR Faculté des Sciences, Département des Sciences de la Terre, Rue de Chartres, BP 6729 , 45067 Orléans cedex 2, France

c. Dipartimento di Geologia, Paleontologia e Geofisica, Università di Padova, Via Giotto 1, 35137 Padova, Italy

Abstract

For axial ratios greater than ~3, natural porphyroclasts from three mylonites all show a very strong SPO with the long axis of the best fit ellipse at an antithetic angle of 5-10° to the shear direction. This is more consistent with a stable end orientation than with the transient or oscillating fabrics predicted by theory for elliptical rigid particles in simple shear. The cause of this divergence from theory was investigated in a series of high simple shear strain ($\gamma > 15$) analogue experiments, performed in a ring-shear machine (couette flow) using a linear viscous matrix (PDMS). The rotational behaviour of rigid elliptical and rhomboidal particles with comparable aspect ratios (~5) to the natural examples was modelled for both coherent and slipping boundaries between particle and matrix. Interface slip causes a dramatic reduction in the rotation rate of the elliptical particle compared to theory, but not stabilization. Interface slip does result in a stable end orientation of the rhomboidal particle, with the long diagonal oriented at a small antithetic angle to the shear direction. For monoclinic particles, mirror image shapes (referred to here as Types 1 and 2) show different rotational behaviour. For the Type 1 particle (with a shape comparable to σ porphyroclast systems), the long side rotates asymptotically into near parallelism with the shear direction. Natural examples of Type 1 particles are hornblende and olivine porphyroclasts measured in mylonites from the Finero Complex, Southern Alps. For Type 2 particles, the short side stabilizes close to the shear direction, or at a small synthetic angle, as also observed for sillimanite pophyroclasts from the Mont Mary mylonites, western Italian Alps. In this natural case, stabilization of the short sides is against an extensional crenulation cleavage

rather than the mylonitic foliation. The analogue experiments establish that slip on the particle interface is one mechanism for stabilization of elongate rhomboidal particles. In natural examples, decoupling from the matrix may be effected by extensional crenulation cleavage or C-planes in S-C fabrics.

Keywords: shear zones, mylonites, rigid particles, shape preferred orientation (SPO), analogue scale models

1. Introduction

Both analytical theory (Jeffery, 1922) and experimental observation (e.g. Ghosh and Ramberg, 1976) predict that elliptical rigid particles embedded in an isotropic, linear viscous matrix undergoing simple shear flow should not develop a stable orientation. However, many natural porphyroclasts formed from strongly anisotropic minerals (e.g. sillimanite, hornblende) have straight faces and are prismatic or rhomboidal in cross-section, rather than elliptical, with an orthorhombic or monoclinic symmetry. In some cases, such porphyroclasts develop a very strong shape preferred orientation in highly sheared rocks (mylonites), which is more characteristic of a stable end orientation than the transient or oscillating fabric expected for continually rotating particles (ten Grotenhuis and Passchier, 1999; Pennacchioni et al., in press). One possibility is that the imposed flow is not simple shear: a component of pure shear results in a stable end orientation for particles above a critical aspect ratio (Ghosh and Ramberg, 1976). Another possibility is that boundary effects (the boundary to the shear zone itself or adjacent stronger layers) cause the stabilization, especially if there is slip at the particle interface (ten Brink and Passchier, 1995; Marques and Coelho, in press). However, it is also possible that the rhomboidal shape itself could promote slip on the long straight faces and such interface slip may significantly modify the rotational behaviour (Ildefonse and Mancktelow, 1993; Odonne, 1994). In particular, in simple shear interface slip could slow down rotation or even stabilize particles in an orientation close to the shear direction (e.g. Ildefonse and Mancktelow, 1993). This study analyses experimentally the rotational behaviour of elliptical and rhomboidal, monoclinic particles with either coherent or slipping boundaries to large values of simple shear ($\gamma > 15$), for comparison with the theoretical Jeffery equation and with natural porphyroclast systems from mylonites.

2. Natural Observations

2.1. Porphyroclast types

Samples from high temperature shear zones at three localities in the Alps are used to illustrate different types of porphyroclast shapes and shape preferred orientations (SPO) occurring in mylonites. Two main monoclinic shapes are distinguished. Type 1 has a geometry similar to σ porphyroclast systems, and Type 2 is the mirror image. A third type of monoclinic porphyroclasts, the well-known mica-fish (e.g. Lister and Snoke, 1984; ten Grotenhuis and Passchier, 1999; Piazolo et al., in press), involve important clast deformation on internal slip planes and are not considered here. The studied mylonites have several common characteristics.

(1) They are high grade rocks deformed under amphibolite facies metamorphic conditions during extensional tectonics.
(2) They retain a large number of porphyroclasts, even though the strain is clearly very high and there has been extensive grain size refinement of the matrix.
(3) Most porphyroclasts have shapes approaching regular geometric forms.
(4) The porphyroclasts have a large range in aspect ratio, reaching up to 1:17 in some samples (*Hbl*[1] in the metagabbro mylonites).

2.2. Type 1 porphyroclasts

2.2.1. The host mylonites

Type 1 porphyroclasts have been found in high temperature mylonites derived from both ultramafics and granulite facies metagabbros of the Finero Complex (Ivrea-Verbano Zone, Italian western Alps).

In ***metagabbros***, the studied shear zone is developed at the contact to peridotites near the village of Provola (coordinates 464.10/5106.4). The shear zone, a few tens of metres thick, involves layered *Hbl-Px-Grt-Pl* gabbros. Mylonites, developed in *Grt*-poor layers, consist of a partly annealed matrix of green *Amph*, *Pl* and *Ilm* containing porphyroclasts of brown *Hbl*, minor *Cpx* and rare *Grt*. The matrix is dominated by a foliation/compositional layering parallel to the shear plane, but under crossed polars a second transverse fabric of matrix amphibole inclined at an antithetic angle of < □ □° to the mylonitic foliation is evident. The mylonitic shear zones developed during amphibolite facies retrogression of the granulite facies metagabbros, under conditions estimated at 650 to 500°C and 0.4-0.6 GPa (Kenkmann and Dresen, 1998; Kenkmann, 2000).

The studied ductile shear zone in ***ultramafics*** is a 50 cm thick ultramylonite with a sharp contact to the adjacent coarse-grained, equigranular phlogopite-bearing peridotite (*Ol*, minor *Opx*, *Phl*, *Hbl, Sp*, *Cpx*). It outcrops along the Cannobino stream, south of the village of Finero (coordinates 464.79/5106.03). In mylonitized ultramafics, porphyroclasts consists mainly of *Ol* and minor *Opx* set in an ultra-fine-grained recrystallized matrix of dominantly *Ol*. Under crossed polars, extinction patterns reveal a composite fabric. Ultramafics and associated mylonites of the Finero complex have been previously studied by Brodie (1980) and Kruhl and Voll (1979a, b), who refer mylonitization to ambibolite facies deformation during retrogression from the granulite facies conditions estimated for the protolith.

2.2.2. Porphyroclast shape

Metagabbro mylonites

In contrast to the Mont Mary mylonites described below, where most of high aspect ratio *Sil* porphyroclasts have a well-developed rhomboidal shape, the shape of elongate porphyroclasts in the Finero mylonites is less regular. This may in part be related to the fact that the long axes of porphyroclasts do not lie perfectly within the XZ plane. However, some porphyroclasts do have shapes ranging from orthorhombic to roughly monoclinic in symmetry. Orthorhombic porphyroclasts cover the range from nearly circular to elliptical to spindle-shaped forms (Fig. 1a). Well-developed *Ilm* pressure shadows are common around the elliptical/circular porphyroclasts (Fig. 1a). Monoclinic particles are generally more elongate (axial ratio $R > 3$), with a shape resembling domains in S-C mylonites (Lister and Snoke, 1984), showing a long roughly straight "C" face and a short "S" face (Fig. 1b). The short faces may be approximately straight, sigmoidal or concave. Sigmoidal short faces give the porphyroclast a typical ship's-prow profile, with one rounded and one pointed connection to the long sides. The porphyroclast tips commonly shows a small *Ilm* pressure shadow (Fig. 1b). Tangents to the short faces form low to high angles (up to nearly orthogonal) with the long sides. The shape is comparable to that of σ-type porphyroclast systems (Passchier and Simpson, 1986) except that, for σ-clasts, the shape refers to both the porphyroclast and the recrystallized mantle. *Hbl* Type 1 porphyroclasts commonly show slight undulose extinction, but there is no sign of strong plastic deformation. A comparison of orthogonal XY, XZ and ZY thin sections

[1] Abbreviations for mineral names follow Kretz (1983).

establishes that elongate *Hbl* porphyroclasts have an approximately prismatic (prolate) shape.

Ultramafic mylonites

The shape of *Ol* porphyroclasts in the ultramafic mylonites is comparable to that of *Hbl* porphyroclasts in the metagabbro mylonites (Fig. 1c). However, *Ol* porphyroclasts commonly show internal plastic deformation features, such as strongly undulose extinction, tabular subgrains and recrystallization. Some porphyroclasts are completely recrystallized to polycrystalline domains. Where recrystallization is not pervasive, it is commonly concentrated close to the short sides. However, the characteristic σ-type shape, as described above, is shown by both polycrystalline and unrecrystallized porphyroclasts. Comparison of orthogonal XY, XZ and ZY thin sections indicates that *Ol* porphyroclasts have a disk or oblate 3-D shape, with the long axis parallel to the Y direction.

2.3. Type 2 porphyroclasts

2.3.1 The host mylonites

Type 2 porphyroclasts are represented by elongate *Sil* in an amphibolite facies (510°-580°C and 0.25-0.45 GPa), water-deficient mylonite derived from paragneisses in the Austroalpine Mont Mary (MM) nappe (Pennacchioni and Cesare, 1997). The MM-mylonites consist of a matrix composed dominantly of *Bt-Qtz-Ilm* and containing numerous porphyroclasts of *Sil*, *Grt* and *Pl*. The fabric in the mylonites (Fig. 1d) is composite and made up of: (1) a mylonitic foliation/compositional banding parallel to the shear plane, (2) a finely spaced extensional crenulation cleavage (ECC), and (3) a SPO of matrix minerals (*Ilm* and *Qtz*) inclined at a synthetic angle of < □□° to (1). ECC often nucleate on, or are pinned to, porphyroclasts. *Sil* geometry and SPO have already been described in detail by Pennacchioni et al. (in press) and are summarized below.

2.3.2. Porphyroclast shape

In MM mylonites, *Sil* has two main shapes: elliptical/circular and rhomboidal (Fig. 1d). They are derived from previous rectangular microboudins common in protomylonites and low strain domains. Elliptical porphyroclasts generally have a relatively low aspect ratio (commonly less than 3). More elongate porphyroclasts are

rhomboidal (monoclinic symmetry) and have short sides parallel to extensional crenulation cleavages (ECC), which is pervasive in some samples. The overall asymmetry of the particle relative to the shear direction (Fig. 1d) is the mirror image of the σ-clasts described above. The rhomboidal shape of *Sil* is common in XZ sections but absent in YZ sections, where *Sil* mainly consists of equant, nearly idioblastic basal sections, with very low interference colours. This indicates that *Sil* porphyroclasts are close to uniaxial in form, with long axes within the XZ plane and close to the stretching direction (X). No sign of internal plastic deformation is present in *Sil* clasts.

2.4. Shape preferred orientation (SPO) of porphyroclasts

2.4.1. SPO measurement

In thin section, a transverse SPO of elongated porphyroclasts inclined at a low antithetic angle to the mylonitic foliation is clearly visible in all three mylonite examples considered here (e.g. Fig. 1d). It is also discernible in hand specimens of both the ultramafic (Fig. 2) and metagabbro mylonites from Finero, due to the millimetric size of most porphyroclasts.

The orientation of the best fit ellipse was measured in three samples representative of the different mylonites. The samples were serially cut to obtain several thin sections (27 for FIN_Gb1: a gabbro mylonite; 9 large thin sections for FIN_Ub1: a ultrabasic mylonite; 16 for MM_06: a paragneiss mylonite) in order to measure a statistically meaningful number of porphyroclasts (988 in FIN_Gb1; 500 in FIN_Ub1; 1913 in MM_06). A few check measurements on other samples taken from the same shear zones show that the SPO measured in the samples discussed here can be reasonably considered representative of the fabric of all the mylonites.

The SPO was measured using NIH Image[2] software on a computer connected to the microscope via a video camera. Orientation was measured with respect to the local foliation since, at the thin section scale, there may be a difference of several degrees in the foliation attitude across a sample. Measured porphyroclasts were marked on enlarged photomicrographs to avoid measuring the same porphyroclast twice. For monoclinic particles, the best fit ellipse determined by NIH does not have its long axis parallel to the longest diagonal of the particle. For example, the discrepancy in the case of the particle shape used for the analogue experiments

described below is 3.7° (see Fig. 5). An SPO determined for such particles would tend to underestimate the antithetic angle by this amount for Type 1 geometry and overestimate it for Type 2. However, since real porphyroclasts rarely have ideal rhomboidal or elliptical cross-sections, there is no practical and efficient alternative for unbiased measurement of the clast orientation.

2.4.2. Results

The cumulative orientation of porphyroclasts measured in the studied mylonite samples is shown in Fig. 3 and the vector mean and strength (Agterberg, 1974) for different axial ratio ranges in Fig. 4. All the mylonites considered here show: (1) a strong R-insensitive SPO oriented at a low antithetic angle (5-10°) to the shear plane for more elongate porphyroclasts (R > ~3); and (2) a much weaker R-dependent SPO oriented approximately parallel to the mylonitic foliation for low aspect ratio porphyroclasts, with the intensity of the SPO decreasing with decreasing R. Despite the observation above that the best fit ellipse may differ by a few degrees from the long diagonal of a perfect rhomboid and that this divergence should be in the opposite sense for Type 1 and 2 particles, there is no significant difference in the measured stable orientation between the Finero and Mont Mary mylonites. The overall effect is clearly small and lost in the statistics of the natural data set, particularly since the porphyroclasts are often transitional between elliptical and rhomboidal shapes.

Considering the relatively variable shape of porphyroclasts in the Finero mylonites and the fact that porphyroclast sides are commonly curved, it is only possible to make a qualitative estimate of the orientation of the different shape elements, such as the porphyroclast long and short faces. In general, however, the long sides of Type 1 elongate porphyroclasts are inclined at a small antithetic angle to or (less frequently) are parallel to the foliation (Fig. 1c).

The more consistent and well-defined shape of *Sil* porphyroclasts in the Mont Mary mylonites allows a more detailed analysis of the SPO characteristics. In particular, the short sides of rhomboidal *Sil* have a constant orientation of 15-17°, parallel to ECC (Fig. 1d), whereas the long sides have a variable orientation increasing from 10° to 16° with a decrease in the aspect ratio from 6 to 3 (see Pennacchioni et al., in press). For these Type 2 particles, it is thus the short side that is

[2] NIH Image analysis software, available at http://rsb.info.nih.gov/nih-image/

stabilized (against ECC), and the variation in orientation of the long side is simply a geometric result of the different aspect ratios.

2.5. Summary of observations on natural porphyroclasts

(1) The shape of elongate porphyroclasts in mylonites is often approximately rhomboidal, with monoclinic symmetry;

(2) With respect to the shear sense, these monoclinic forms are of two types. Type 1 has a geometry like typical σ-clasts, whereas Type 2 is the mirror image. Both forms can be found in natural mylonites, due to the different mechanisms of clast generation.

(3) In the mylonites studied, all monoclinic particles (which, in general, are more elongate than the elliptical particles, i.e. with R usually > 3) develop a strong preferred shape orientation with the long axis of the NIH Image best fit ellipse inclined at a low antithetic angle (5-10°) to the shear foliation. This angle is independent of the particle aspect ratio.

(4) This strong SPO independent of both strain magnitude and aspect ratio suggests a stable end orientation for the more elongate (R > 3) rigid particles in the mylonites. This observation is not explained by existing theories for rotation of an elliptical rigid particle with coherent boundaries in an isotropic linear viscous matrix. As a first step to understanding the natural behaviour, the influence of monoclinic particle shape and interface slip was therefore investigated in a series of analogue scale-model experiments.

3. Experimental Methods

The experiments consider the behaviour of elongate rigid particles in a linear viscous matrix undergoing simple shear (couette flow). The matrix material is a transparent polydimethyl-siloxane polymer (PDMS sold by Dow Corning USA as SGM 36), which has been used in many other scale-model experiments (e.g. Passchier and Simpson, 1986; Weijermars, 1986; Arbaret et al., 2001; Marques and Coelho, in press). For the experimental shear strain rates (~ 7 x 10^{-4} s^{-1} at the particle location) and temperature (~22°C), PDMS is linear viscous with a viscosity of ~ 5 x 10^{4} Pa s (Passchier and Simpson, 1986; Weijermars, 1986). Particles were constructed from polyethylene, which has a density of 0.91, only slightly less than that of PDMS (0.97), so that gravitational effects were not significant for the experiment duration

(mostly < 12 hours). The particles used in the experiments are cylindrical or right-regular with the cylindrical axis parallel to the particle rotation axis in simple shear flow. The 2D particle shapes and dimensions are given in Fig. 5. As noted above, for monoclinic shapes there are two distinct mirror-image possibilities for the orientation of the particle relative to the shear sense, referred to as Type 1 and Type 2.

The length of the third particle dimension (cylindrical axis), which is 2.07 cm for the rhomboid and 2.05 cm for the ellipse, does not have an important influence on the rotational behaviour (Arbaret et al., 2001). Particle dimensions are small compared to the 12 cm width of the sheared matrix ring (e.g. see Fig. 17), so that stabilization effects due to the boundaries, as already modelled by Marques et al. (in press), are avoided. For slipping interfaces, lubrication was achieved with an initial ~1-1.5 mm thick mantle of liquid soap on the sides and base of the particle (Marques and Coelho, in press).

For simple shear of a linear viscous material, the rotation rate $\dot{\theta}$ of a cylindrical rigid particle with an elliptical cross-section is given by (Jeffery, 1922; Ghosh and Ramberg, 1976):

$$\dot{\theta} = \frac{\dot{\gamma}}{R^2 + 1}\left[R^2 \sin^2 \theta + \cos^2 \theta\right] \qquad (1)$$

where R is the aspect ratio of the ellipse, $\dot{\gamma}$ the far field simple shear strain rate, and θ is the angle between the long axis of the ellipse and the shear direction. The rotation rate oscillates between a maximum when the long axis is perpendicular to the shear direction and a minimum when it is parallel. As R increases, the rotation rate when close to the shear direction may be so slow that the particle can appear to be stabilized in that position for quite large values of shear strain. For example, an elliptical particle with an axial ratio of 5 (similar to that used in this study) requires a shear strain of γ = 16.3 to complete a 180° rotation and has its long axis within ±10° of the shear strain direction for a γ range of ~ 7.5. Any investigation of possible particle stabilization must therefore be carried out to large shear strain. For this reason, a ring-shear rig was employed for which the there is no limit to the shear strain that can be obtained.

The machine is the same as that used by Arbaret et al. (2001) and is similar in principle to that of Passchier and Sokoutis (1993) and ten Brink and Passchier (1995), but of larger size. Couette flow produced by cylindrical ring shear involves a radial gradient in shear strain that depends on the rheology of the material employed. The

gradient can be minimized by decreasing the gap between the cylinders relative to the radius. An analytical expression relating the shear strain rate ($\dot{\gamma}$) to the distance from the rotation axis (r) for a linear viscous material in couette flow (Reiner, 1960; Masuda et al., 1995) is given by:

$$\dot{\gamma} = \frac{-2\left(\Omega_i - \Omega_e\right)}{\frac{1}{r_i^2} - \frac{1}{r_e^2}} \frac{1}{r^2}, \qquad (2)$$

where r_e and r_i are the radii and Ω_e and Ω_i the angular velocities of the external and internal boundaries respectively. In the ring-shear rig used here, the outer (r_e) and inner (r_i) radii of the cylinders are 30 cm and 18 cm respectively (fig. 1 in Arbaret et al., 2001). Calibration experiments have established that the analytical expression closely describes the observed behaviour of PDMS at experimental strain rates in this rig (fig. 3 in Arbaret et al., 2001).

A regular grid was imprinted on the upper surface of the PDMS using a partially fixed photocopy. The grids were later digitized from photographs to allow the displacement and strain fields to be calculated. This is only possible in the initial stages because of the extreme distortion at higher shear strains.

4. Results

4.1. Elliptical Particle with Non-Slipping Boundaries

This case is considered first as a standard for comparison because the experimental conditions are consistent with the assumptions made in 2D Jeffery theory (except that in the ring-shear apparatus there is a radial gradient in shear strain rate). In Fig. 6, the measured rotation of the long axis of the elliptical particle (with R = 5.3) for duplicate experiments is plotted against the shear strain (calculated with Eq. 2 at the centre of the particle) and compared with theoretical curves calculated with Eq. 1. The experimental behaviour deviates slightly but consistently from theory at high strain. There is an increase in the total rotation for a particular shear strain, similar to that expected for a particle with a slightly lower axial ratio (of ~ 5.1, see Fig. 6).

4.2. Monoclinic Particle with Non-Slipping Boundaries

The rotational behaviour of the Type 1 monoclinic particle is presented in Fig. 7 and for Type 2 in Fig. 8. The behaviour is practically identical to that predicted by

Jeffery theory for an ellipse with its long axis parallel to the long diagonal of the rhomboid (see also Arbaret et al., 2001; Piazolo et al., in press), with an aspect ratio of 5.65 for the Type 1 particle and 5.45 for the Type 2 particle. In other words, the Type 1 particle rotates more slowly than Type 2. Note that the R-values corresponding to the best fit theoretical curves for both Type 1 and Type 2 particles (5.65 and 5.45, respectively) are considerably higher than the R value of 4.4 for the best fit NIH Image ellipse (Fig. 5c, e).

The perturbation in displacement and in the magnitude of finite strain and rotation for the initial stages of these two experiments, when the long axis is at a high angle to the shear direction, are plotted in Figs. 9 and 10. The patterns for the two experiments are effectively identical. Perturbations in the displacement form closed loops (e.g. Cobbold, 1975; Abbassi and Mancktelow, 1990; Mancktelow, 1991). The finite strain shows two conjugate bands of lower strain, one of which is parallel and the other oblique to the shear direction (Figs. 9c, 10c). Two corresponding zones of decreased and increased finite rotation also occur parallel and oblique to the shear direction respectively (Figs. 9b, 10b). For comparison, the corresponding plots for a Type 2 monoclinic particle when the long axis is close to the shear direction are given in Fig. 11. The pattern to the perturbation in the rotation (Fig. 11b) is similar to that in Figs. 9b and 10b, but the perturbation in the background flow is minor in comparison to the cases considered above, with only a small region of reduced finite strain localized around the particle itself (Fig. 11c). The matrix itself is little disturbed and only the noise involved in digitization is apparent. It follows that the disturbance in the matrix varies as the particle rotates and that, as might be expected, the maximum disturbance in the flow occurs when the long axis is at 90° and the minimum when it is parallel.

4.3. Elliptical Particle with Slipping Boundaries

The introduction of a lubricated interface around the elliptical particle dramatically reduces the rate of rotation but does not result in stabilization (Fig. 12). Whereas for non-slipping boundaries a 180° rotation required a shear strain of ~16.5 (Fig. 6), with slipping boundaries it required 28.3, which is the shear strain theoretically necessary for a complete rotation of an elliptical particle with axial ratio 8.9. However, the experimental rotation data of Fig. 12 does not plot exactly on the theoretical curve for a particle with aspect ratio 8.9 and includes different stages of

rotation behaviour. There is an initial period ($\gamma < 10$) when the particle long diagonal asymptotically approaches a (quasi-) stable orientation at around -14° (i.e. antithetic with regard to the shear sense), followed by a period of more steady rotation. It could be argued that the transition at $\gamma \sim 10$, from a tendency to stabilize to one of continued rotation, corresponds to sticking at the boundaries as the soap mantle was thinned by progressive shearing. To test this, the experiment was reversed overnight. Rather than an increased rotation rate during reversal, as expected if sticking across the boundaries had been partly re-established, the overall rotation rate was actually slower during reversal. The difference was only small, however, and broadly speaking the rotational behaviour of the lubricated elliptical particle appears to be reversible.

There is also a significant difference in positional history of the non-slipping and slipping elliptical particles (Fig. 13). In the duplicate, non-slipping experiments the particle centre remained within ± 1 mm of its initial position. There is perhaps a minor tendency to move into the higher strain region closer to the inner cylinder during rotation into an orientation parallel to the shear direction and to move out again as the angle of the long axis to the shear direction increases again. There may also be some memory effect, with a weak tendency to overall translation outwards during cycles of rotation. In comparison, this pattern of movement is much more strongly developed for the slipping particle (Fig. 13a). As a result, the strain rate varies at the particle centre during rotation (Fig. 13b) and Fig. 12 was constructed by integrating the strain rate history (using a best-fit 5^{th} order polynomial function) rather than assuming a constant strain rate equivalent to the initial position. Again there may be a memory effect, with cycles of rotation moving the particle gradually outward, since during the reverse experiment the position when returned to the starting 90° orientation was 4 mm further out. However, properly testing this possibility would require additional duplicate experiments involving multiple cycles of rotation (i.e. γ on the order of 100 or more).

4.4. Monoclinic Particle with Slipping Boundaries

The behaviour of rhomboidal particles with lubricated boundaries is shown in Figs. 14 (Type 1) and 15 (Type 2). In both cases the introduction of slip at the particle-matrix interface results in stabilization, but with different rotational histories and final orientations for the two particle types.

The Type 1 particle rotates asymptotically toward a stable orientation with the long side parallel to the shear direction. The particle follows the theoretical curve of an equivalent ellipse of aspect ratio 5.65 in the initial stage up to $\gamma \sim 2$, at which time the particle long diagonal makes an angle of ~20° to the shear direction (and consequently the particle long sides an angle of ~10°). From this position onward, the rotation rate slows down dramatically with respect to the theoretical curve and the particle asymptotically approaches a stable position with the long side parallel to the shear direction. In this orientation, the long diagonal is inclined at ~11° to the shear direction.

The Type 2 particle shows a more complex behaviour. Two experiments were run under identical conditions to check for data reproducibility. In both runs, the particle initially rotates through the position with the short side parallel to the shear direction without any apparent influence, following the theoretical curve for an equivalent ellipse of aspect ratio 5.45. However, soon afterwards the particle rotation rate decreases compared with theory and the particle stabilizes transiently, with the long diagonal making an angle of ~12-14° to the shear direction in experiment (a) and ~16° in (b). After $\gamma \sim$ 5.5-6, the particle again rotates synthetically with the applied shear until $\gamma \sim$ 7-8, at which stage the long diagonal is at an angle of 4° in (a) and 10° in (b) to the shear direction. From this position the particle then begins to back-rotate asymptotically toward an orientation with the short side parallel to the shear direction (in experiment a) or still making a small (~5°) synthetic angle with the shear direction (in experiment b). Overall, in both experiments the long diagonal of the particle lies within 5 to 20° of the shear direction (in an antithetic sense) for $\gamma > 3$ (and at least up to γ = 20-28, the upper limit of the experiments).

Similar to the behaviour of the slipping elliptical particle, the rhomboidal particles are displaced toward the inner cylinder as the long diagonal rotates toward the shear direction. As the orientation stabilizes, the particles continue to move steadily inward into the higher strain rate region (Fig. 16). This is the important difference from the elliptical particle. It did not stabilize and during continued and accelerating rotation away from the shear direction, the particle centre moved out again. The rhomboidal particles do not rotate through the shear direction and the particle is translated steadily inward.

Detachment along the boundary of the rhomboidal particles leads to displacement of the fold packets developed at the ends of the particle out into the

matrix (Fig.17). As a result, isolated fold packets may be preserved at a considerable distance form the nucleating rigid inclusion and in natural examples, the direct connection to the initiating particle may no longer be preserved.

5. Discussion

5.1 *Control Experiment: Elliptical Particle with Non-Slipping Boundaries*

The elliptical particle shows a rotational behaviour very similar to theoretical prediction, but rotates slightly faster than expected (Fig. 6). This can only reflect the gradient in shear strain inherent in the ring-shear rig. Intuitively, it is perhaps expected that a shear gradient should promote rotation rather than stabilization. At least in this study, any observed stabilization is therefore contrary to machine effects and must be due to other more fundamental causes.

5.2 *Effect of Particle Shape on the Rotational Behaviour in Experiments*

Many experimental studies have stressed the minor effect of the exact particle shape on its rotational behaviour, with the shape being well approximated by an enveloping ellipse with its major axis parallel to the longest particle dimension (e.g. fig. 8 in Arbaret et al., 2001). This general applicability of the simplified theoretical model for ellipsoidal forms to a wide range of particle shapes reflects the fact that an adjoining volume of matrix rotates with the particle, together forming an approximately ellipsoidal object (fig. 11 in Arbaret et al., 2001). The current study again confirms that this assumption may hold to a first approximation for a “no-slip" condition at the particle/matrix interface. However, in detail, even in the case of non-lubricated boundaries, the shape and symmetry of the particle with respect to the shear sense exert some influence on particle rotation. In particular, it is remarkable that the monoclinic Type 1 particle rotates more slowly than Type 2. This is probably because Type 1 particles have the long straight side close to the shear direction when the long diagonal is at a small antithetic angle to the shear direction, whereas for Type 2, it is the short side. Even without discernible discrete slip on the interface, the presence of straight boundaries is therefore having some influence on the adjacent matrix flow, with a (minor) tendency for overall slower rotation rate when long straight segments are close to the shear direction.

Lubrication of particle boundaries has a profound effect on particle kinematics for both elliptical and monoclinic particles. However, stabilization only occurs for the monoclinic shape with straight sides, at least for the aspect ratio of ~5 considered in

the current experiments. The critical role of the orientation of long straight sides, as noted above for non-lubricated particles, is evident in Type 1 particles, which rotate asymptotically into an end orientation with the long side parallel to the shear direction. The situation is more complicated and less clear-cut in the case of the Type 2 particle. The duplicate experiments do differ in detail, most likely reflecting slightly different stick/slip behaviour at the particle matrix interface as the soap layer is progressively thinned during continued shear. However, the overall history of particle rotation for the two experiments is broadly similar and in this case it is the short side that comes to lie nearly parallel to the shear direction, perhaps with some tendency (in experiment b) to make a small synthetic angle with the shear direction.

5.3 *Radial Displacement of the Particle*

Overall, there is a tendency for the particle to move inward when rotating toward the orientation with the long axis parallel to the shear direction and outward when rotating away from this position. The effect is discernible but weak for experiments with a non-slipping particle/matrix interface and probably reflects the unequal force couple on the particle due to the radial strain-rate gradient inherent in the ring shear rig. The effect is very apparent for the experiments with slipping boundaries for which a stable end-orientation is attained, with the centre of the particle moving steadily inward. As can be seen from Fig. 17, at high strain the particle lies within a thin highly elongated layer of the lubricant soap that originally formed an even mantle surrounding the particle. The thin layer is a material surface and progressive passive deformation of this material surface will decrease the angle it makes with the inner cylinder. It follows that a material point on this surface, such as the centre of the particle, must migrate inwards. This effect, if dependent on the passive rotation of the soap layer, should be reversible, as demonstrated in Fig. 12.

5.4 *Comparison between experimental and natural behaviour*

Two facts are established above: (1) in at least some natural shear zones, monoclinic rigid particles with axial ratios above a critical value of ~3 approach a stable end orientation; and (2) in analogue experiments, slip on the interface of monoclinic particles also produces stabilization. The question remains whether the experimental results provide the explanation for the natural observations. In other words, is it slip (or concentrated shear) at the particle interface that causes

stabilization in the natural examples or some other factor (e.g. boundary effects, a component of pure shear, non-linear or anisotropic rheology etc.). For the Mont Mary mylonites, it is the short side of the rhomboidal *Sil* porphyroclasts that is stabilized, as in the experiments for comparable Type 2 particles. However, stabilization occurs not against the shear direction but against ECC. In this case, the observational evidence does indeed suggest that concentrated shear nucleating on the particle interface is primarily responsible for stabilization (albeit not in exactly the same orientation as attained in the experiments). For the more irregularly shaped, approximately Type 1 (i.e. sigmoidal) porphyroclasts from the Finero mylonites, the case is less clear. Some porphyroclasts do show indications of discrete shear horizons on the longer sides (e.g. Fig. 1b), similar to C planes in S-C mylonites. However, the stable orientation does not seem to be that with the long side strictly parallel to the shear direction, but rather slightly oblique in an antithetic sense. This is consistent with the experiments, where even at high γ, the long side still makes a small antithetic angle with the shear direction. However, the natural angle seems to be slightly larger than expected at very large shear strain ($\gamma > 20$) from the experiments.

One notable difference between the experiments and the natural examples is the lack of complex fold patterns in the matrix, due to the disturbed flow around the rigid particles (Fig. 17, see also van den Driessche and Brun, 1987; Ildefonse and Mancktelow, 1993). As noted above, the fold packets may be transported away from the immediate vicinity of the particle by discrete shear on slip surfaces, but even such isolated fold packets seem to be lacking in the matrix of the mylonites (Fig. 1). The fold packets may not be preserved if the matrix is continually recrystallizing during progressive shear but compositional banding, as seen in Fig. 1d, could still be expected to preserved some memory of the distubance in flow around the rigid inclusions. This difference between experiment and natural observation remains unexplained.

6. Conclusions

(1) A rigid elliptical particle with axial ratio 5.3 embedded in a homogeneous, isotropic, Newtonian linear-viscous matrix rotates continuously for simple shear flow. For non-slipping boundaries, the rotation rate is slightly less than that predicted from the equation of Jeffery (1922), presumably due to the shear gradient in the ring-shear

machine. Slip at the boundaries slows the rotation rate dramatically but a stable end-orientation is not attained.

(2) Rigid monoclinic rhomboidal particles (axial ratio R = 4.4 for the NIH Image best fit ellipse) with non-slipping boundaries also do not attain a stable orientation for simple shear flow. The variation in rotational rate with orientation is identical in form to the classic Jeffery (1922) solution for elliptical particles. Type 1 (σ-type) particles rotate slightly more slowly than Type 2 (inverse σ-type) particles.

(3) For slipping boundaries, the same particles reach a stable orientation. For Type 1 particles, the long side is stabilized parallel to the shear direction (i.e., the long diagonal makes an antithetic angle of ~11°). For Type 2 particles, the rotational history is more complex but, starting from an initial perpendicular orientation, the long diagonal remains within 5 to 20° of the shear direction, in an antithetic sense, for $\gamma > 3$, and the particle orientation is effectively stabilized.

(4) The centre of the rigid particle is displaced toward the inner cylinder (i.e., into the higher strain rate region) as the long axis rotates into parallelism with the shear direction. The longer this orientation is maintained, the greater the displacement. The monoclinic particles with slipping boundaries, which attain a stable orientation, are continuously displaced in this direction.

(5) Natural examples of Type 1 σ-clasts from mafic and ultramafic mylonites in the Finero Complex of the Ivrea-Verbana Zone, Southern Alps, and Type 2 inverse σ-clasts from paragneiss mylonites, Mont Mary, western Alps, both show stabilization above a critical R of ~3, with the long dimension at a small antithetic angle (5-10°) to the shear direction. For Type 1 particles, the long side is either near parallel or at a low antithetic angle to the mylonitic foliation, similar to the experimental results. For Type 2 clasts, the short sides are oriented at a constant synthetic angle of 15-17° to the shear direction and appear to be stabilized against EEC.

(6) The experiments establish that slip or concentrated shear on rigid particle boundaries is a potential mechanism to explain the observed strain-insensitive shape preferred orientation of some natural porphyroclast systems in high strain mylonites.

Acknowledgements

Thanks to Giulio di Toro, who was involved in measurement of the Mont Mary mylonites and to Robert Hofmann for construction of the ring-shear machine.

References

Abbassi, M.R., Mancktelow, N.S., 1990. The effect of initial perturbation shape and symmetry on fold development. Journal of Structural Geology 12, 273-282.

Agterberg, F.P., 1974. Geomathematics; Mathematical Background and Geo-Science Applications. Developments in Geomathematics 1. Elsevier Scientific Publishing, Amsterdam, 596 pp.

Arbaret, L., Mancktelow, N.S., Burg, J.-P., 2001. Effect of shape and orientation on rigid particle rotation and matrix deformation in simple shear flow. Journal of Structural Geology 23, 113-125.

Brodie, K.H., 1980. Variations in mineral chemistry across a shear zone in phlogopite peridotite. Journal of Structural Geology 2, 265-272.

Cobbold, P.R., 1975. Fold propagation in single embedded layers. Tectonophysics 27, 333-351.

Ghosh, S.K., Ramberg, H., 1976. Reorientation of inclusions by combination of pure shear and simple shear. Tectonophysics 34, 1-70.

Ildefonse, B., Mancktelow, N.S., 1993. Deformation around rigid particles: the influence of slip at the particle/matrix interface. Tectonophysics 221, 345-359.

Jeffery, G.B., 1922. The motion of ellipsoidal particles immersed in a viscous fluid. Proceedings of the Royal Society of London, Series A 102, 161-179.

Kenkmann, T., 2000. Processes controlling the shrinkage of porphyroclasts in gabbroic shear zones. Journal of Structural Geology 22, 471-487.

Kenkmann, T., Dresen, G., 1998. Stress gradients around porphyroclasts: palaeopiezometric estimates and numerical modelling. Journal of Structural Geology 20, 163-173.

Kretz, R., 1983. Symbols for rock-forming minerals. American Mineralogist 68, 277-279.

Kruhl, J.H., Voll, G., 1979a. Excursion-guide to the western part of the Finero peridotite-metagabbro-complex of the Ivrea Zone (N-Italy). Proceedings of the 2nd symposium Ivrea-Verbano, Istituto de Geologia e Mineralogia, Universita di Padova, Italy, pp. 17-26.

Kruhl, J.H., Voll, G., 1979b. Deformation and metamorphism of the western Finero Complex. Proceedings of the 2nd symposium Ivrea-Verbano, Istituto de Geologia e Mineralogia, Universita di Padova, Italy, pp. 95-109.

Lister, G.S., Snoke, A.W., 1984. S-C mylonites. Journal of Structural Geology 6, 617-638.

Mancktelow, N.S., 1991. The analysis of progressive deformation from an inscribed grid. Journal of Structural Geology 13, 859-864.

Marques, F.O., Coelho, S., in press. Rotation of rigid elliptical cylinders in viscous simple shear flow: analogue experiments. Journal of Structural Geology.

Masuda, T., Mizuno, N., Kobayashi, M., Nam Tran, N., Otoh, S., 1995. Stress and strain estimates for Newtonian and non-Newtonian materials in a rotational shear zone. Journal of Structural Geology 17, 451-454.

Odonne, F., 1994. Kinematic behaviour of an interface and competence contrast: analogue models with different degrees of bonding between deformable inclusions and their matrix. Journal of Structural Geology 16, 997-1006.

Passchier, C.W., Simpson, C., 1986. Porphyroclast systems as kinematic indicators. Journal of Structural Geology 8, 831-843.

Passchier, C.W., Sokoutis, D., 1993. Experimental modelling of mantle porphyroclasts. Journal of Structural Geology 15, 895-909.

Pennacchioni, G., Cesare, B., 1997. Ductile-brittle transition in pre-Alpine amphibolite facies mylonites during evolution from water-present to water-deficient conditions (Mont Mary Nappe, Italian Western Alps). Journal of Metamorphic Geology 15, 777-791.

Pennacchioni, G., Di Toro, G., Mancktelow, N.S., in press. Strain-insensitive preferred orientation of porphyroclasts in Mont Mary mylonites. Journal of Structural Geology.

Piazolo, S., ten Grotenhuis, S.M., Passchier Cees, W., in press. A new apparatus for controlled general flow modeling of analog materials. In: H.A. Koyi and N.S. Mancktelow (Editors), Tectonic Modeling: A Volume in Honor of Hans Ramberg. GSA Memoir 193.

Reiner, M., 1960. Deformation, Strain, and Flow: An Elementary Introduction to Rheology. Lewis & Co. Ltd, London, 347 pp.

ten Brink, C.E., Passchier, C.W., 1995. Modelling of mantled porphyroclasts using non-Newtonian rock analogue materials. Journal of Structural Geology 17, 131-146.

ten Grotenhuis, S.M., Passchier, C.W., 1999. Mica fish and other fish-shaped shear sense indicators. Terra Abstracts 11, 828.

van den Driessche, J., Brun, J.P., 1987. Rolling structures at large shear strain. Journal of Structural Geology 9, 691-704.

Weijermars, R., 1986. Flow behaviour and physical chemistry of bouncing putties and related polymers in view of tectonic laboratory applications. Tectonophysics 124, 325-358.

Figure Captions

Fig. 1 Photomicrographs of measured natural porphyroclasts in mylonites from three localities in the Alps. (a) Range of porphyroclast shapes in metagabbro mylonite from Finero. (b) Elongate Type 1 sigmoidal *Hbl* porphyroclast in metagabbro mylonite from Finero. (c) Sigmoidal Type 1 *Ol* porphyroclast in the ultramafic mylonite from Finero. (d) Type 2 rhomboidal porphyroclasts of prismatic *Sil*, showing a strong SPO. Note the ECC in an orientation parallel to the constantly oriented short sides of the *Sil* porphyroclasts.

Fig. 2 Ultramafic mylonite from Finero showing the clear SPO of *Ol* porphyroclasts already discernible in hand specimen.

Fig. 3 Axial ratio R versus orientation of the best fit NIH Image ellipse for all porphyroclasts measured in the studied mylonite samples. Note the very strong SPO developed at an antithetic angle of 5-10° to the shear direction for R > ~3. Note also that above this critical R value the SPO is not dependent on R.

Fig. 4 Mean vector orientation versus vector strength (Agterberg, 1974) for different axial ratio ranges corresponding to Fig. 3.

Fig. 5 Dimensions of the rigid polyethylene particles used in the experiments. (a) elliptical particle of thickness 2.05 cm (b) rhomboidal particle of thickness 2.07 cm. Type 1 geometry for sinistral shear. An ellipse of ratio 5.65 is also shown (see Fig. 7). (c) Type 1 particle with the NIH best-fit ellipse (R = 4.4) indicated. Note that the long axis of this ellipse is oblique at an angle of 3.7° to the long diagonal of the particle. (d) Type 2 geometry for sinistral shear (mirror image of (b)). An ellipse of ratio 5.45 is also shown (see Fig. 8). (e) Type 2 particle with the NIH best-fit ellipse indicated.

Fig. 6 Rotational behaviour of the long axis of an elliptical particle with axial ratio 5.3 and non-slipping boundaries, in sinistral ring shear (results form two identical experiments, note the excellent reproducibility). The particle rotates

more rapidly through the shear direction than expected from theory (Jeffery, 1922) (the theoretical curve for R = 5.3 is shown as a solid line).

Fig. 7 Rotational behaviour of the long diagonal of a Type 1 monoclinic particle in sinistral ring shear. The particle rotates like an elliptical particle with axial ratio 5.65 and long axis parallel to the long diagonal.

Fig. 8 Rotational behaviour of the long diagonal of a Type 2 monoclinic particle in sinistral ring shear. The particle rotates like an elliptical particle with axial ratio 5.45 and long axis parallel to the long diagonal. This ratio is smaller than for Fig. 7, indicating a slightly faster overall rotational behaviour for this shape.

Fig. 9 Plots of (a) the perturbation displacement field, (b) contours of the difference in finite rotation angle, and (c) contours of the difference in finite strain for a particle of Type 1 initially at ~45° to the shear direction (cf. Fig. 7). For (b) and (c), the difference between measured finite and theoretical homogeneous values are plotted. In (a), the average orientation of the particle between initial and final steps is given, in (b) and (c) it is the final orientation. Calculated homogeneous shear strain value at the particle centre is $\gamma = 2.1$.

Fig. 10 Plots of (a) the perturbation displacement field, (b) contours of the difference in finite rotation angle, and (c) contours of the difference in finite strain for a particle of Type 2 initially at ~45° to the shear direction (cf. Fig. 8). For (b) and (c), the difference between measured finite and theoretical homogeneous values are plotted. In (a), the average orientation of the particle between initial and final steps is given, in (b) and (c) it is the final orientation. Calculated homogeneous shear strain value at the particle centre is $\gamma = 0.8$.

Fig. 11 Plots of (a) the perturbation displacement field, (b) contours of the difference in finite rotation angle, and (c) contours of the difference in finite strain for a particle of Type 2 initially near parallel to the shear direction. For (b) and (c), the difference between measured finite and theoretical homogeneous values are plotted. In (a), the average orientation of the particle between initial and

final steps is given, in (b) and (c) it is the final orientation. Calculated homogeneous shear strain value at the particle centre is $\gamma = 1.0$.

Fig. 12 Rotational behaviour of the long axis of an elliptical particle with axial ratio 5.3 and slipping boundaries (thin mantle of liquid soap), in sinistral ring shear. Both forward and reverse experiments are indicated. Measurements were only taken for the latter part of the reverse experiment.

Fig. 13 Effect of boundary slip on radial translation of the elliptical particle during shear. (a) Location relative to the inner cylinder. The non-slipping particle remains more-or-less in the same position, whereas the slipping particle first moves in toward the inner cylinder as the long axis approaches the shear direction and then out again as the long axis rotates toward the 90° orientation. (b) Corresponding change in theoretical strain rate at the centre of the particle. (c) Rotational history of the particle for comparison.

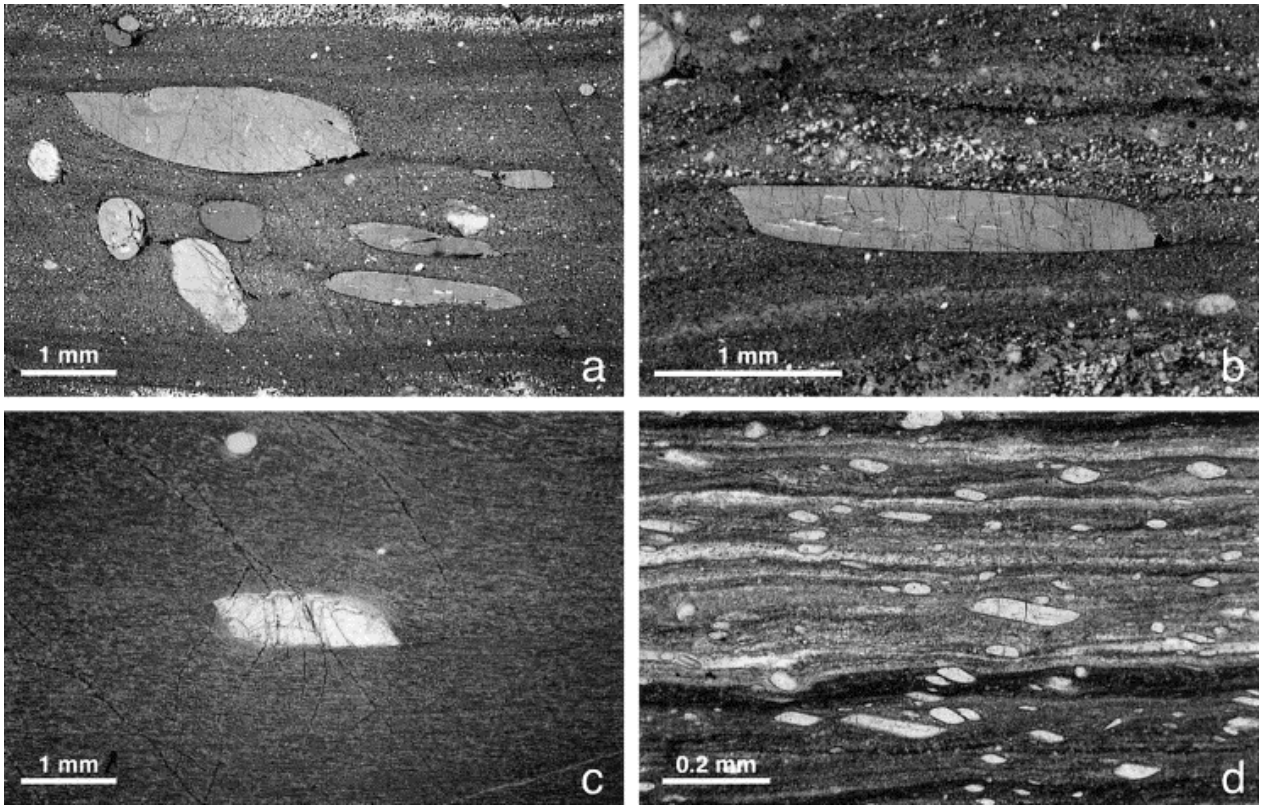
Fig. 14 Rotational behaviour of the Type 1 monoclinic particle with slipping boundaries (thin mantle of liquid soap), in sinistral ring shear. The long side of the particle rotates asymptotically toward the shear direction, with the result that the long diagonal rotates toward a direction making an antithetic angle of ~ 11° to the shear direction.

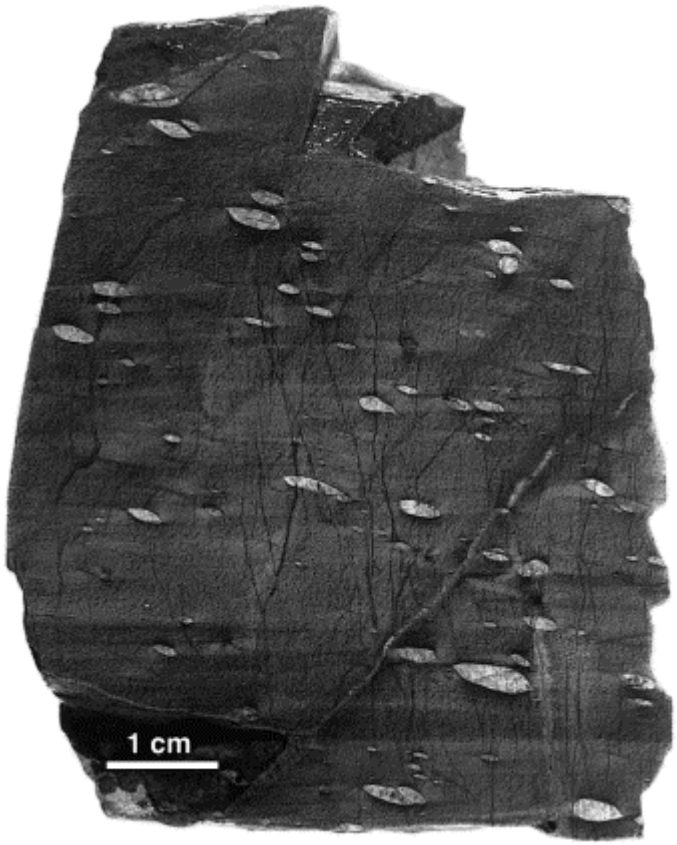
Fig. 15 Rotational behaviour of a Type 2 monoclinic particle with slipping boundaries (thin mantle of liquid soap), in sinistral ring shear. Duplicate experiments (a) and (b) produced slightly different results. In (a) the short side eventually stabilizes parallel to the shear direction. In (b) the apparently stable end orientation has the short side oriented at a small angle of ~5° to the shear direction.

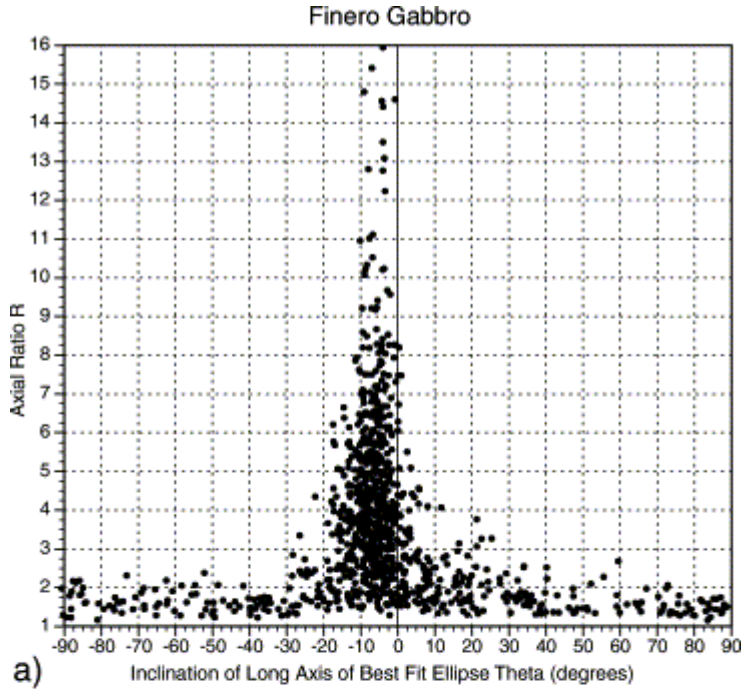
Fig. 16 Effect of boundary slip on radial translation of the monoclinic rhomboidal particle during shear. The behaviour is similar for Type 1 and 2 particles. The results for the Type 2 particle are presented here, corresponding to Fig. 8 and Fig. 15b for the non-slipping and slipping cases respectively. (a) Location relative to the inner cylinder. The non-slipping particle remains

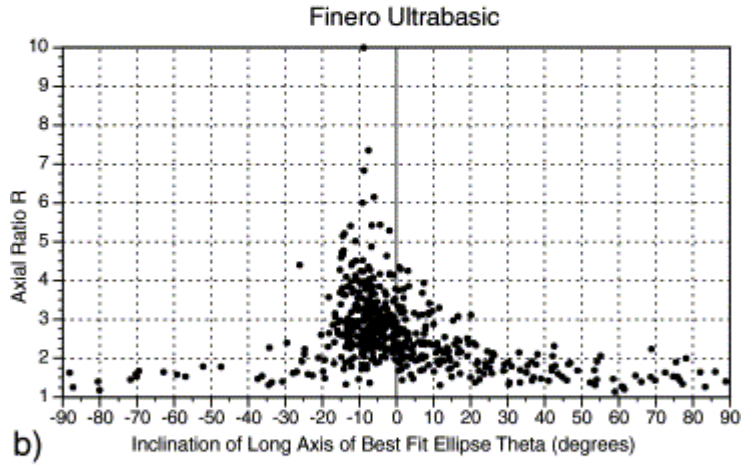
more-or-less in the same position, whereas the slipping particle moves steadily toward the inner cylinder. (b) Corresponding change in theoretical strain rate at the centre of the particle. (c) Rotational history of the particle for comparison.

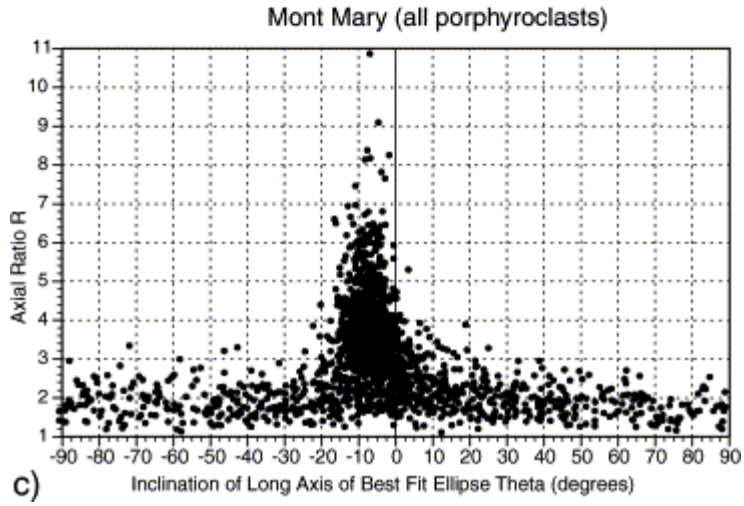
Fig. 17 Deformed grid around rhomboidal particles in a stable orientation. (a) Type 1 particle for γ = 15.6 at the particle centre (see Fig. 14), and (b) Type 2 particle for γ = 15.5 at the particle centre (see Fig. 15a).

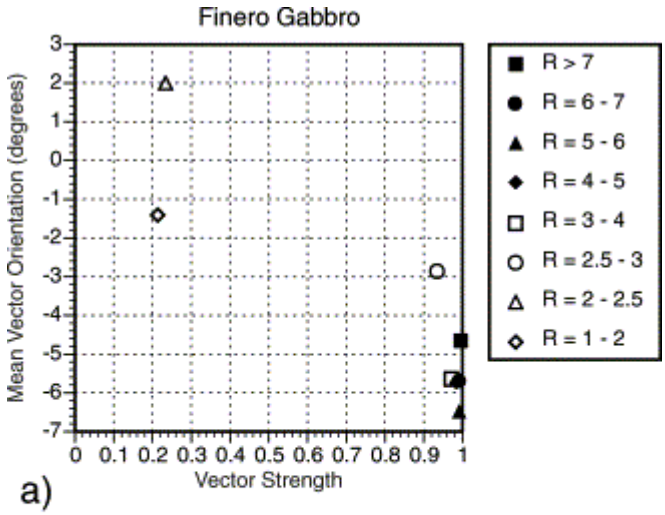

1 mm
a
1 mm
b
1 mm
c
0.2 mm
d


1 cm

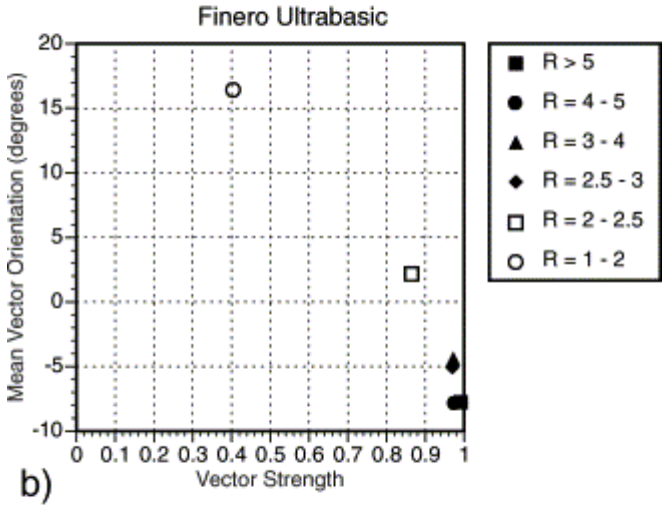

Finero Gabbro
Axial Ratio R
Inclination of Long Axis of Best Fit Ellipse Theta (degrees)
a)


Finero Ultrabasic
Axial Ratio R
Inclination of Long Axis of Best Fit Ellipse Theta (degrees)
b)

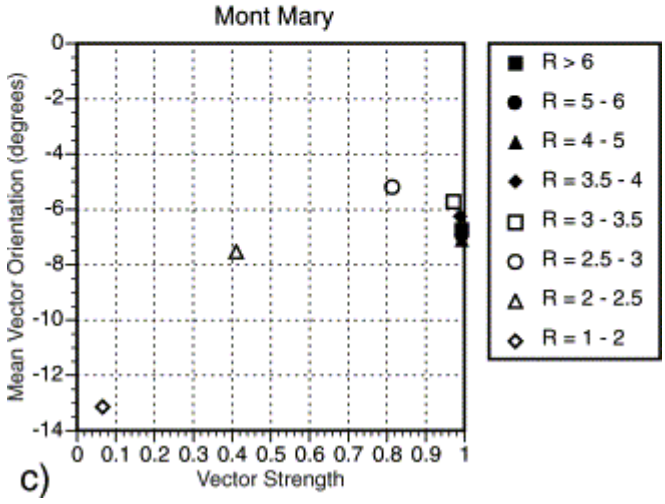

Mont Mary (all porphyroclasts)
Axial Ratio R
Inclination of Long Axis of Best Fit Ellipse Theta (degrees)
c)


Finero Gabbro
Mean Vector Orientation (degrees)
Vector Strength
R > 7
R = 6 - 7
R = 5 - 6
R = 4 - 5
R = 3 - 4
R = 2.5 - 3
R = 2 - 2.5
R = 1 - 2

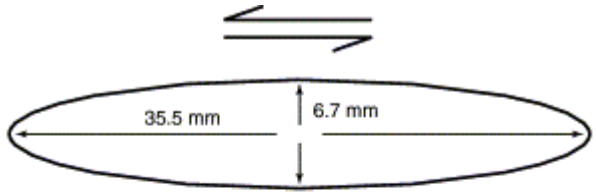
a)


Finero Ultrabasic
Mean Vector Orientation (degrees)
Vector Strength
R > 5
R = 4 - 5
R = 3 - 4
R = 2.5 - 3
R = 2 - 2.5
R = 1 - 2

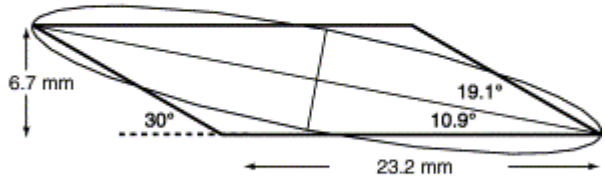
b)


Mont Mary
Mean Vector Orientation (degrees)
Vector Strength
R > 6
R = 5 - 6
R = 4 - 5
R = 3.5 - 4
R = 3 - 3.5
R = 2.5 - 3
R = 2 - 2.5
R = 1 - 2

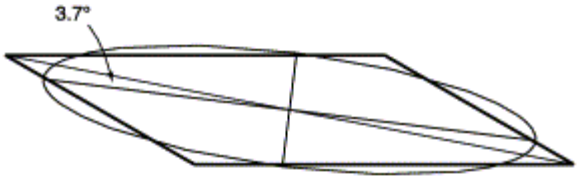
c)



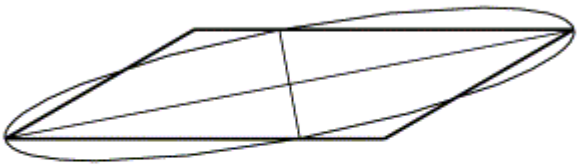
a) Elliptical particle with axial ratio 5.3



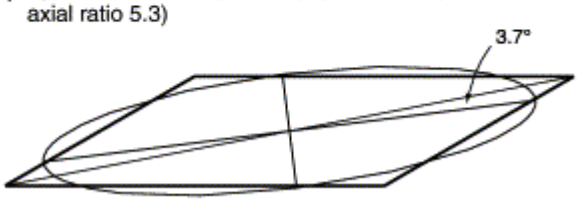
b) Type 1 monoclinic particle (equivalent ellipse with axial ratio 5.65)



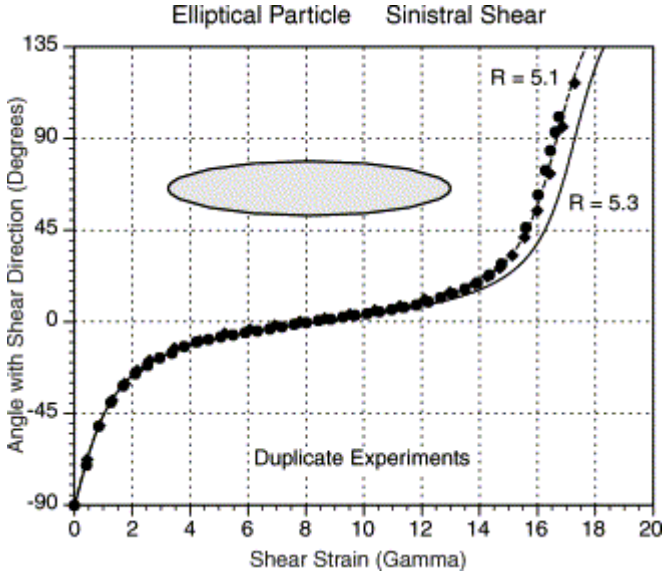
c) Type 1 monoclinic particle (NIH best fit ellipse axial ratio 4.4, weakly oblique to diagonal)

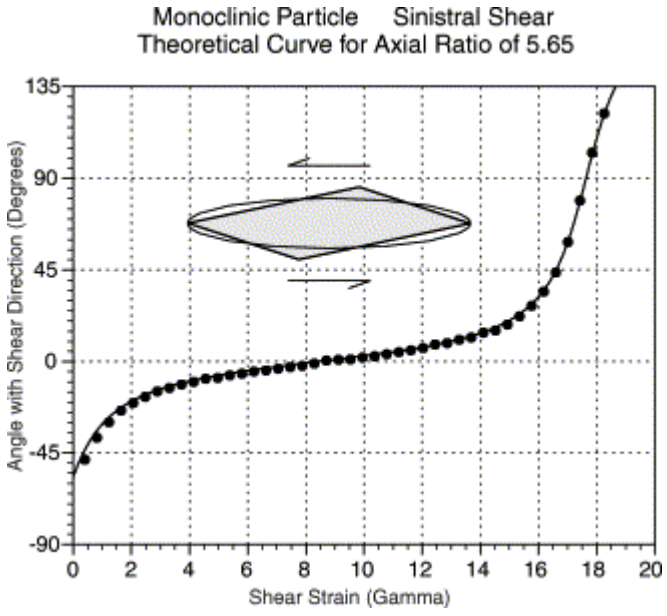


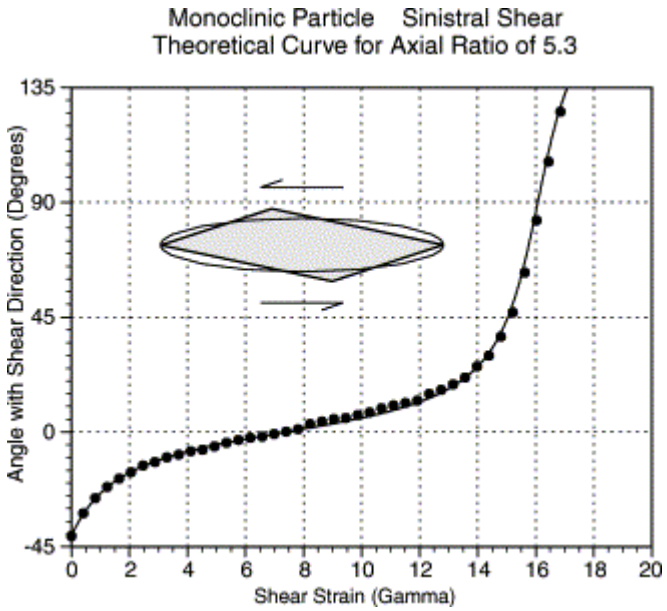
d) Type 2 monoclinic particle (equivalent ellipse with axial ratio 5.3)

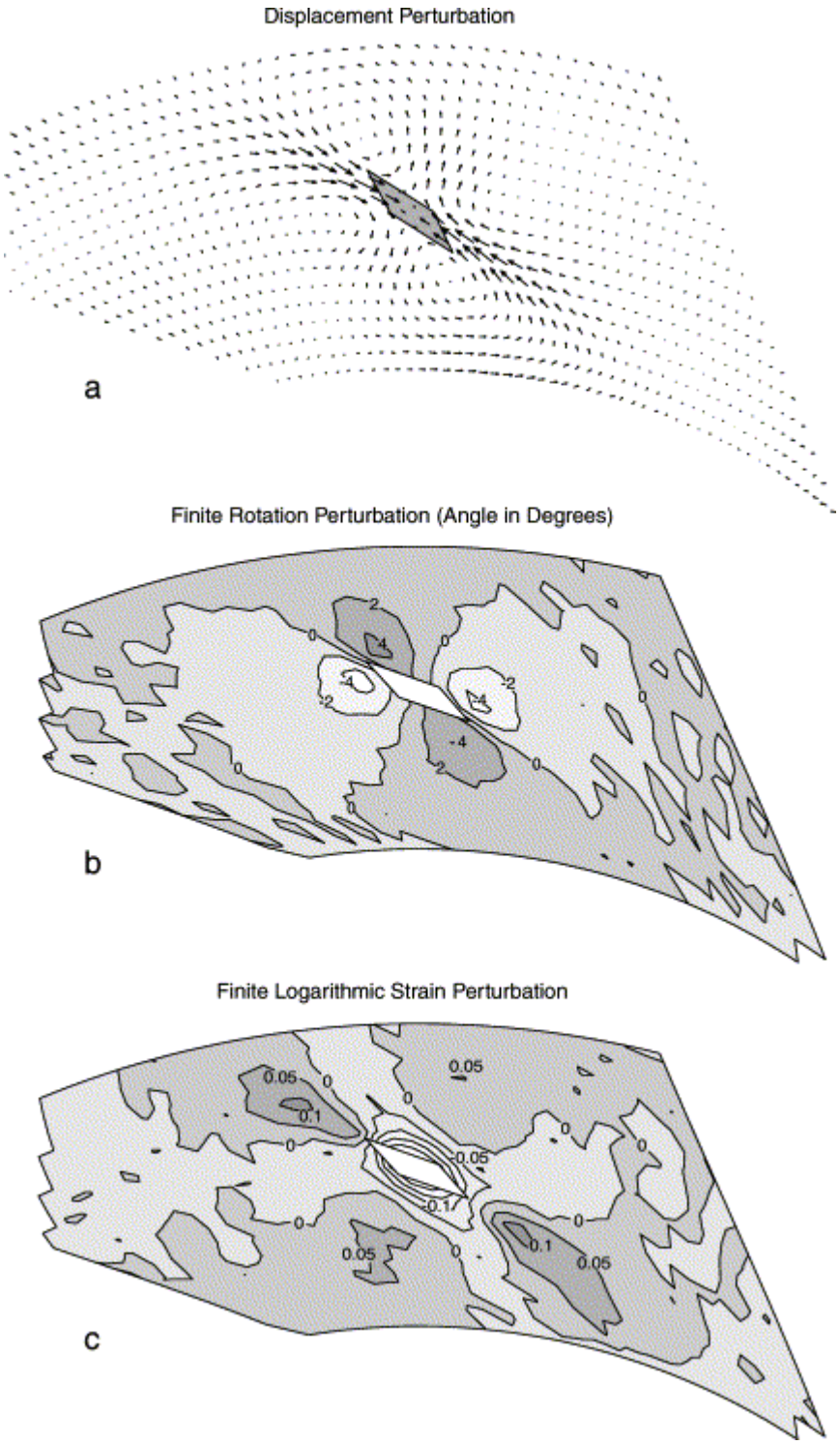


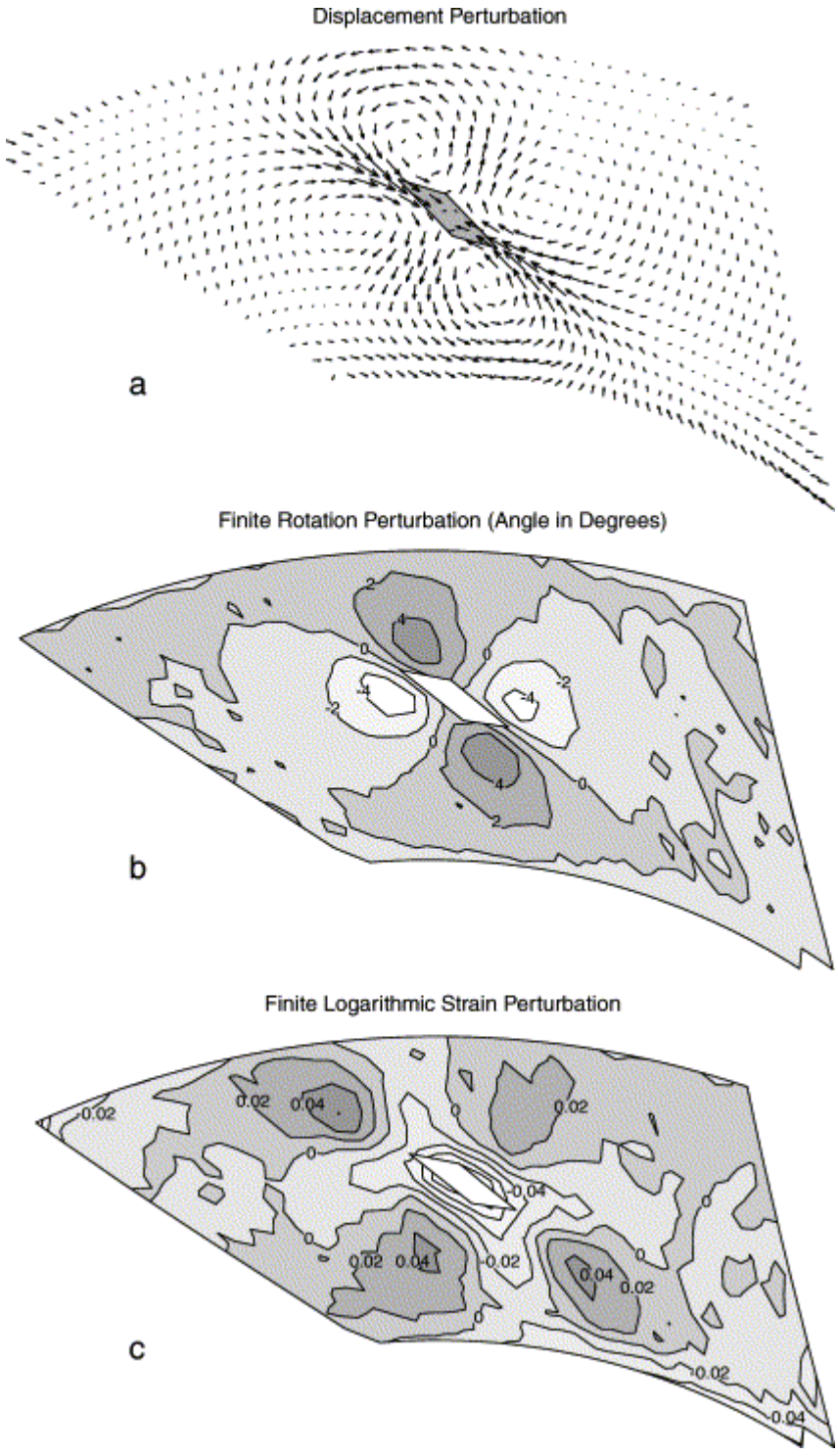
e) Type 2 monoclinic particle (NIH best fit ellipse axial ratio 4.4, weakly oblique to diagonal)

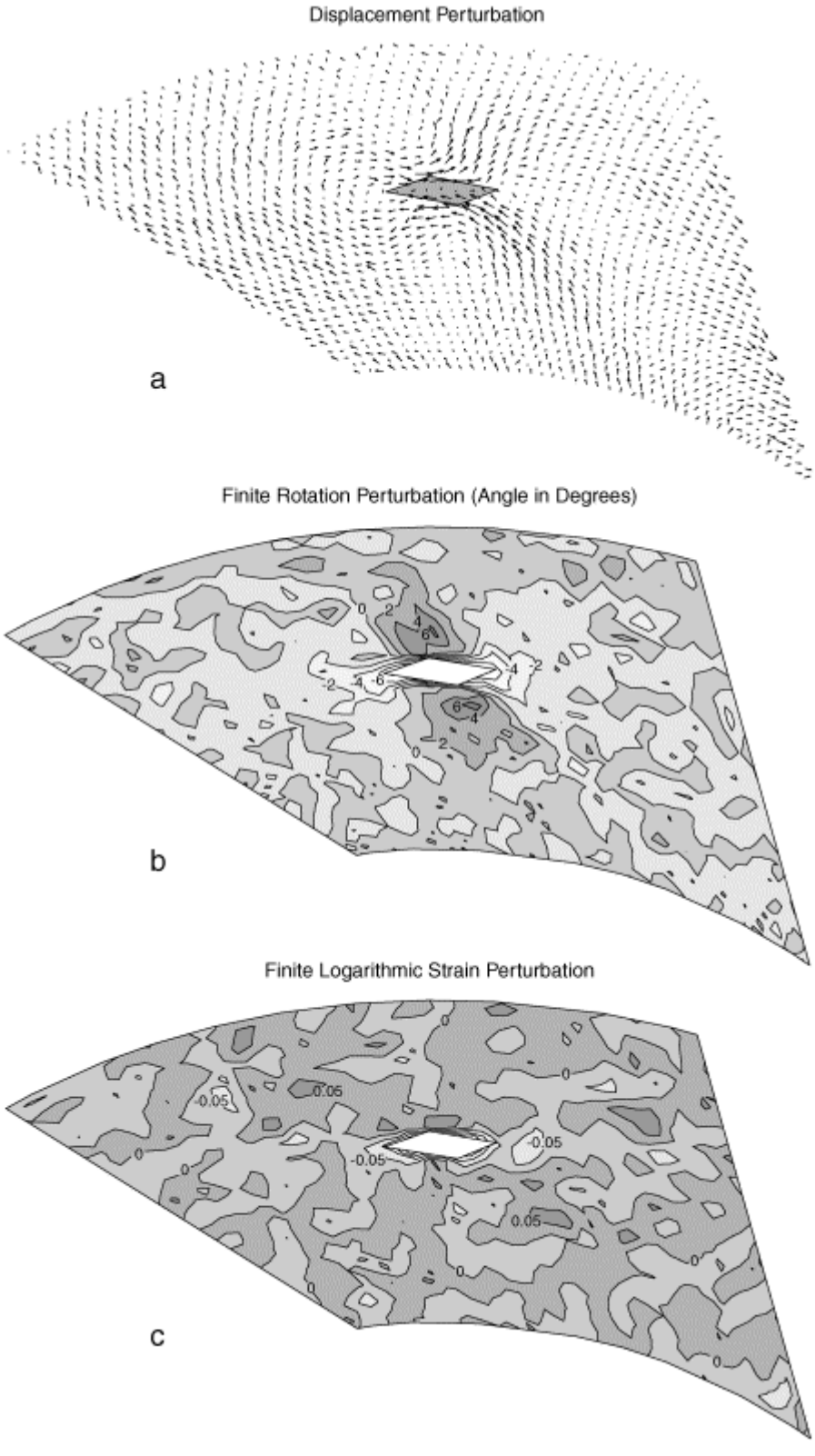

Elliptical Particle Sinistral Shear
R = 5.1
R = 5.3
Duplicate Experiments
Angle with Shear Direction (Degrees)
Shear Strain (Gamma)
135
90
45
0
-45
-90
0
2
4
6
8
10
12
14
16
18
20

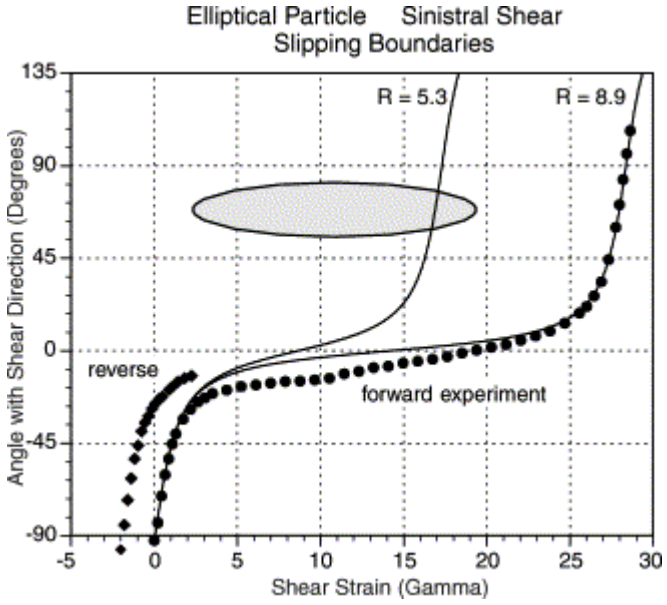

Monoclinic Particle Sinistral Shear
Theoretical Curve for Axial Ratio of 5.65
Angle with Shear Direction (Degrees)
Shear Strain (Gamma)
135
90
45
0
-45
-90
0
2
4
6
8
10
12
14
16
18
20

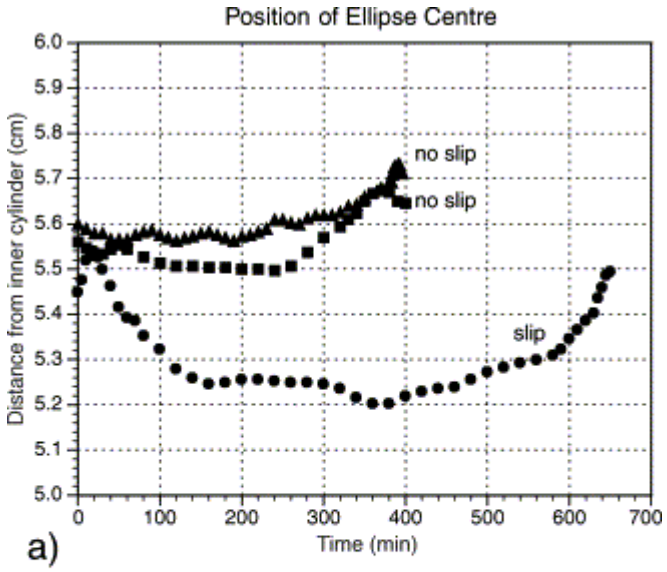

Monoclinic Particle Sinistral Shear
Theoretical Curve for Axial Ratio of 5.3
Angle with Shear Direction (Degrees)
135
90
45
0
-45
0
2
4
6
8
10
12
14
16
18
20
Shear Strain (Gamma)


Displacement Perturbation
a
Finite Rotation Perturbation (Angle in Degrees)
2
0
4
-4
-2
-2
4
0
-4
2
0
0
b
Finite Logarithmic Strain Perturbation
0.05
0
0.1
0
0.05
0
0
0.05
0.1
0
0.05
0
0.1
0.05
c

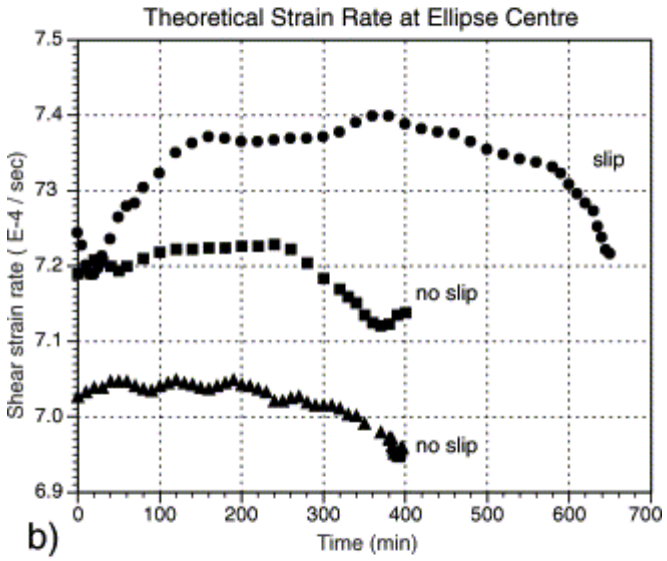

Displacement Perturbation
a
Finite Rotation Perturbation (Angle in Degrees)
b
Finite Logarithmic Strain Perturbation
c


Displacement Perturbation
a
Finite Rotation Perturbation (Angle in Degrees)
b
Finite Logarithmic Strain Perturbation
c

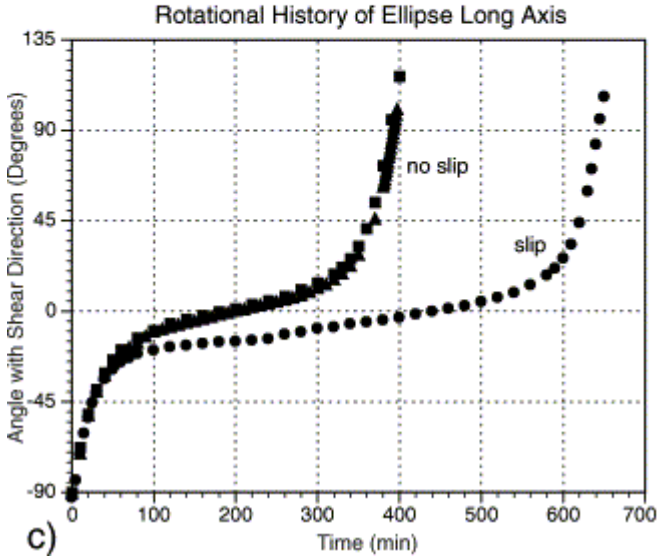

Elliptical Particle Sinistral Shear
Slipping Boundaries
R = 5.3
R = 8.9
reverse
forward experiment
Angle with Shear Direction (Degrees)
Shear Strain (Gamma)
135
90
45
0
-45
-90
-5
0
5
10
15
20
25
30


Position of Ellipse Centre
Distance from inner cylinder (cm)
6.0
5.9
5.8
5.7
5.6
5.5
5.4
5.3
5.2
5.1
5.0
no slip
no slip
slip
0
100
200
300
400
500
600
700
Time (min)

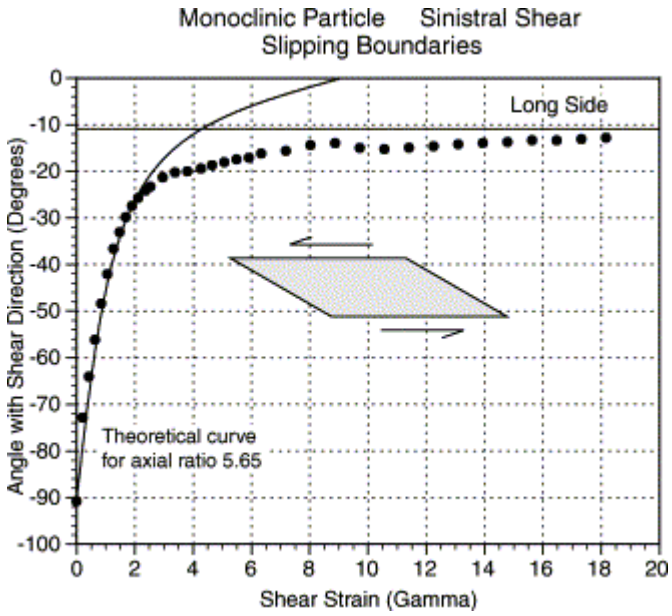
a)

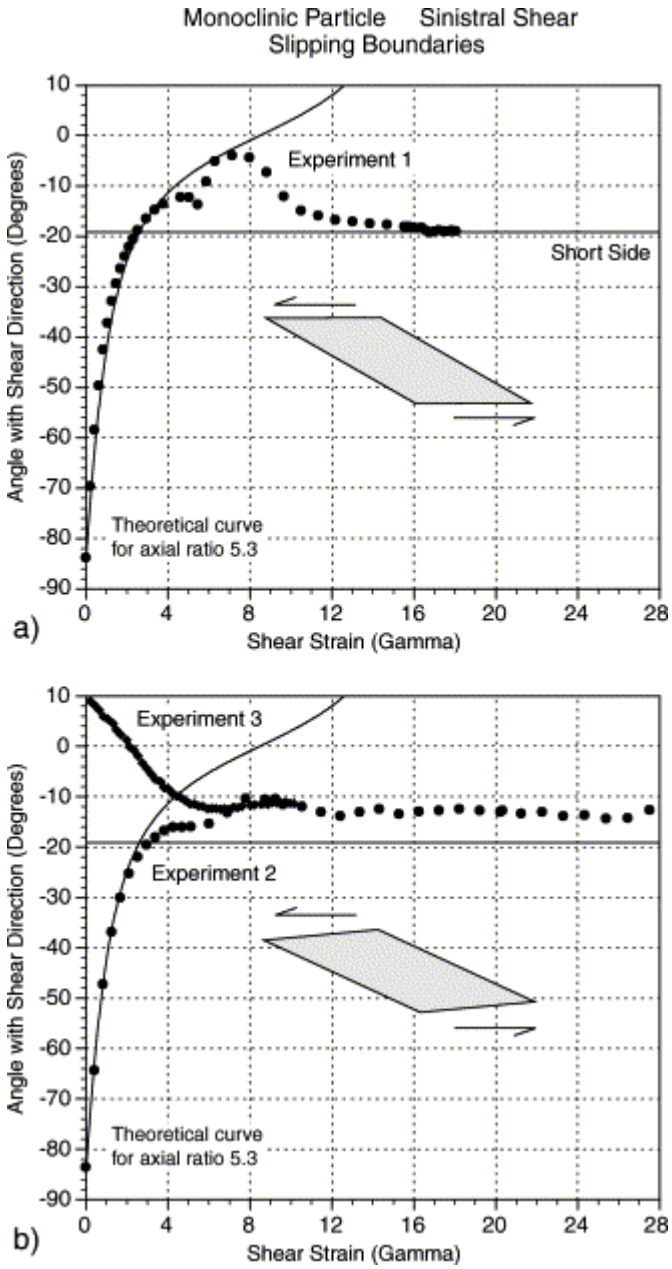

Theoretical Strain Rate at Ellipse Centre
Shear strain rate (E-4 / sec)
7.5
7.4
73
7.2
7.1
7.0
6.9
slip
no slip
no slip
0
100
200
300
400
500
600
700
Time (min)

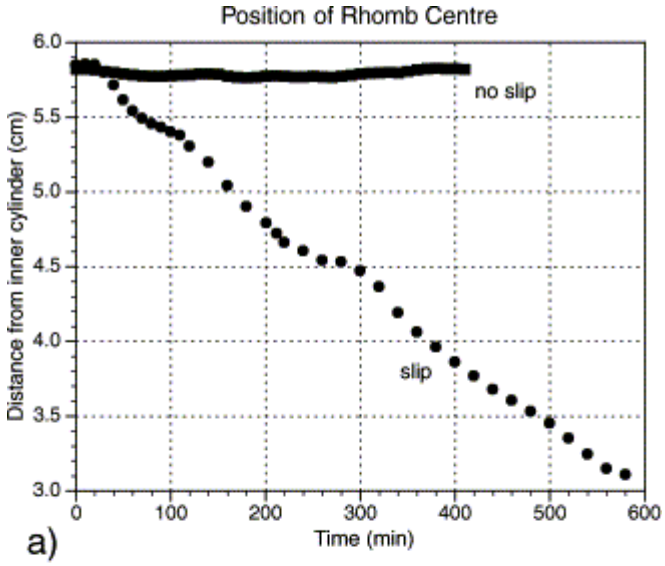
b)

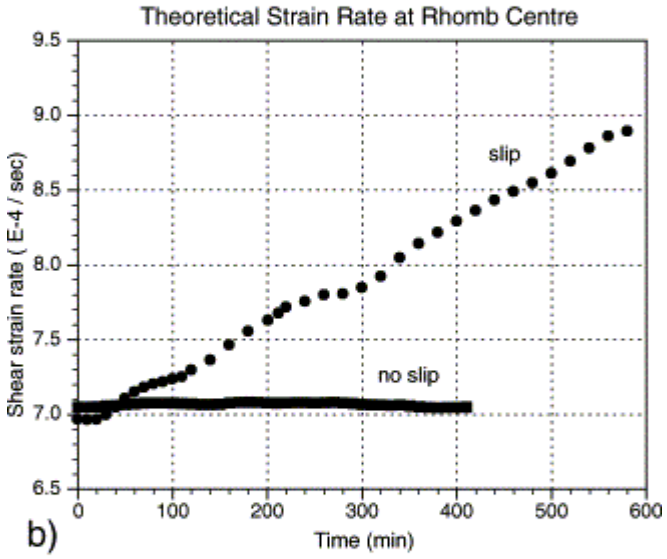

Rotational History of Ellipse Long Axis
Angle with Shear Direction (Degrees)
135
90
45
0
-45
-90
no slip
slip
0
100
200
300
400
500
600
700
Time (min)

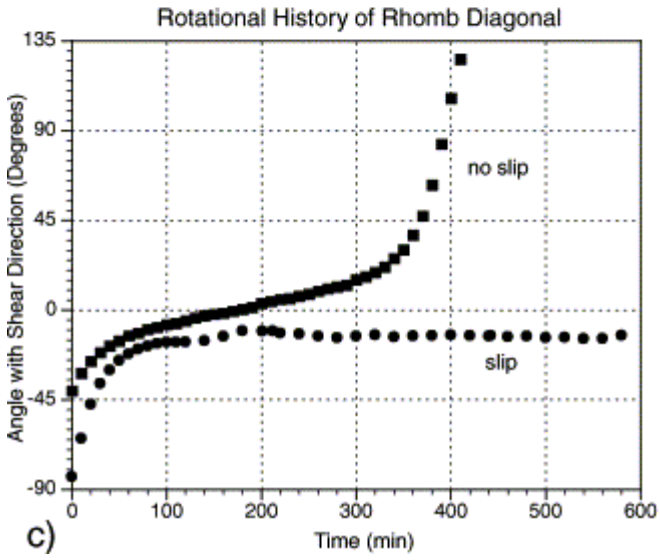
c)


Monoclinic Particle Sinistral Shear
Slipping Boundaries
Long Side
Theoretical curve
for axial ratio 5.65
Angle with Shear Direction (Degrees)
Shear Strain (Gamma)
0
-10
-20
-30
-40
-50
-60
-70
-80
-90
-100
0
2
4
6
8
10
12
14
16
18
20


Monoclinic Particle Sinistral Shear
Slipping Boundaries
Angle with Shear Direction (Degrees)
Shear Strain (Gamma)
Experiment 1
Short Side
Theoretical curve
for axial ratio 5.3
a)
Experiment 3
Experiment 2
Theoretical curve
for axial ratio 5.3
b)


Position of Rhomb Centre
Distance from inner cylinder (cm)
Time (min)
no slip
slip
a)


Theoretical Strain Rate at Rhomb Centre
Shear strain rate (E-4 / sec)
Time (min)
slip
no slip
b)


Rotational History of Rhomb Diagonal
Angle with Shear Direction (Degrees)
Time (min)
no slip
slip
c)


a
b